


Cite this: *RSC Adv.*, 2020, 10, 44503

# New accurate molecular dynamics potential function to model the phase transformation of cesium lead triiodide perovskite (CsPbI<sub>3</sub>)

Saeed S. I. Almishal  and Ola Rashwan \*

Inorganic metallic halide perovskites and cesium lead triiodide, CsPbI<sub>3</sub>, in particular, have gained enormous attention recently due to their unique photovoltaic properties and low processing temperatures. However, their structural stability and phase transition still need an in-depth investigation to better optimize their optoelectronic properties. For sake of time and cost, Classical Molecular Dynamics (CMD) and first principles calculations are being used to predict the structure stability and phase transition of CsPbI<sub>3</sub>. The major challenge of CMD is the choice of proper interatomic potential functions. In this paper, a new hybrid force field is being introduced, which integrates the embedded atomic potentials of Cs–Cs and Pb–Pb with Buckingham–Coulomb potentials. The Buckingham–Coulomb interatomic potential was solely employed as well. The outputs from both force fields were reported and compared to the experimental values. In fact, the new Hybrid Embedded Atomic Buckingham–Coulomb (EABC) potential reproduces, with a great degree of accuracy (within 2.5%), the structural properties, such as the radial distribution functions, interatomic separation distances, and the density. Also, it detects the phase transformation from an orthorhombic into a cubic crystal structure and the melting temperature at 594 K and 750 K respectively which agrees with the experimental values to within 1%. The new proposed hybrid potential proved to be accurate so it could potentially be used to infer the structure stability and the mechanical and thermal properties of the pure inorganic halide perovskites and the mixed halide perovskites as well which are used in various applications.

Received 3rd October 2020  
Accepted 18th November 2020

DOI: 10.1039/d0ra08434d

rsc.li/rsc-advances

## Introduction

Halide perovskites are gaining huge attention for being very promising not only for photovoltaic applications<sup>1</sup> but for other applications as well. They offer various new structures with superior properties that can be used in high-pressure applications<sup>2</sup> and low-cost and flexible memory devices.<sup>3</sup> Halide perovskite solar cell efficiency has rapidly increased through the recent years from 2.2% in 2006 to 25.2% which has been reported recently.<sup>4</sup>

Halide perovskites have an ABX<sub>3</sub> chemical formula, where A is a monovalent cation, B is a metal divalent cation and X is a halide anion. The archetypal perovskite of this family is methylammonium lead triiodide (MAPbI<sub>3</sub>) which has been studied intensively. Solar cells based on MAPbX<sub>3</sub> are highly attractive for their high absorption coefficient, tunable bandgap, low carrier recombination, and easy fabrication.<sup>5</sup> The methylammonium (MA) cations cause complex dynamics because of their molecular orientation, molecular entropy and loss of stability.<sup>6</sup> The choice of the A cations is important as it significantly influences the light absorption in the visible

spectrum.<sup>7</sup> Therefore, the MA cations could be substituted with larger cations, such as Cs<sup>+</sup> or Rb<sup>+</sup> for higher stability without sacrificing the optoelectronic properties as the lead halide sublattice is responsible for the direct bandgap.<sup>6,7</sup>

Recently, cesium lead triiodide (CsPbI<sub>3</sub>) has been getting attention along with the family of mixed halides of CsPb(I<sub>x</sub>Br<sub>1-x</sub>)<sub>3</sub>.<sup>8</sup> CsPbI<sub>3</sub> is an inorganic halide perovskite where a cesium cation (Cs<sup>+</sup>) replaces the methylammonium cation (MA<sup>+</sup>) of MAPbI<sub>3</sub>. It has a more stable structure and unique photovoltaic properties. The black cubic polymorph of CsPbI<sub>3</sub> ( $\alpha$ -CsPbI<sub>3</sub>) with *Pm* $\bar{3}$ *m* structure and 1.73 eV bandgap, is the one used for the photovoltaic applications and was reported experimentally to be stable at a temperature higher than 593.15 K.<sup>9</sup>

To better understand the effect of the temperature on the stability of the structure and the phase transition of inorganic halide perovskites over a relatively long-time, Classical Molecular Dynamics (CMD) is more favorable compared to the Density Functional Theory (DFT). Although there were numerous studies that used various first principles methods to understand the stability and electronic properties of halide perovskites,<sup>10–12</sup> these methods are computationally expensive and unsuitable for large systems. Additionally, the stability of the structure over a relatively long time and various temperatures could not be effectively predicted by these methods.

Penn State Harrisburg, USA. E-mail: ola.rashwan@psu.edu



Classical Molecular Dynamics (CMD) offers a solution to model such large systems by treating the atomic movement classically through Newton's laws.<sup>13–15</sup> The availability and transferability of force fields, that describe the interatomic interactions among the compound constituents, pose a challenge in using CMD. Force fields are usually obtained by finding the proper fitting parameters that could reproduce the experimental structural properties, such as density and interatomic distances. These parameters are usually generated by first principle quantum mechanics calculations or empirical methods.<sup>13</sup>

In classical molecular dynamics, the total energy  $E_{\text{total}}$  of the system is represented as the sum of all interactions between all the atoms in the system as shown in eqn (1)

$$E_{\text{total}} = \sum_{i < j}^N E_2(r_i, r_j) + \sum_{i < j < k}^N E_3(r_i, r_j, r_k) + \dots \quad (1)$$

where  $N$  is the total number of atoms in the system,  $r_i$ ,  $r_j$  and  $r_k$  are the atomic positions of the atoms  $i$ ,  $j$ , and  $k$ , respectively.  $E_2$  and  $E_3$  are the contributions to the total energy from distinct pairs and triplets, respectively.<sup>13</sup> Considering only the energy contribution of distinct pairs, eqn (1) was reduced to eqn (2)

$$E_{\text{total}} = \sum_{i < j}^N E_2(r_i, r_j) \quad (2)$$

where  $E_{\text{total}}$  now represents the pair atomic potentials. Lennard Jones (LJ) and Buckingham (B) potentials are the most common types of pair atomic potentials used in studying halide perovskites.<sup>13,15</sup>

The first hybrid potential to model  $\text{MA}^+$  based perovskites was developed by Mattoni *et al.*,<sup>16</sup> 'MYP', by fitting on data from *ab initio* models. In MYP model, the inorganic–inorganic potential parameters were rescaled to Matusi  $\text{MgSiO}_3$  parameters.<sup>17</sup>  $\text{MA}^+$  ( $\text{CH}_3\text{NH}_3^+$ ) was represented by the standard GAFF force field that includes bonded interactions. (Pb–I) and (C–N) interactions were modelled by Buckingham–Coulomb-potential while (H–Pb) and (H–N) interactions were modelled by Coulomb–LJ potential. They also assumed that the interaction between C–Pb is the same as N–Pb and they both resemble Cs–Pb in  $\text{CsPbI}_3$ , and the same applies to C–I and N–I for Cs–I. The MYP fitting parameters were further enhanced by refining the  $\text{MA}^+$  atomic partial charges and the interactions of Pb–I to reproduce the density functional theory DFT calculations of the cohesive energy, Pb–I distortion energy, molecules re-orientation energy and bulk modulus of a hydrostatic deformed cubic crystal. Further, the N–I interaction was refined to ensure the orthorhombic-to-tetragonal transition.<sup>16,18</sup>

Mattoni *et al.*<sup>16</sup> proved that the MYP calculations meet the experiments and DFT results on the important structural and vibrational properties of the material, such as energy as a function of lattice spacing.<sup>16</sup> In studying the phase transition, the potential produced the general features of the transition from the orthorhombic crystal structure to the tetragonal structure and to the cubic crystal structure. Nevertheless, MYP was also used to determine the sources of phase transition in  $\text{MAPbI}_3$  which are mainly attributed to the dynamic behavior of organic cations in the lead iodide lattice.<sup>19</sup> The MYP was further

employed in studying the diffusion of point defects and it showed that the dominant mechanism of ionic transport in  $\text{MAPbI}_3$  is iodine diffusion.<sup>20</sup>

For its acceptable accuracy, the MYP force field was used to study the behavior of different phases of  $\text{MAPbI}_3$  under various conditions. It was used to model the nucleation and interfacial mismatch during the vapor deposition of  $\text{MAPbI}_3$  on the  $\text{TiO}_2$  substrate.<sup>21</sup> It was also used to study phonon scattering,<sup>22</sup> carrier mobility,<sup>23</sup> polaronic strain,<sup>24</sup> and the qualitative characterization of the nature and the relaxation properties of the dielectric polarization.<sup>25</sup> The use of MYP was not limited to 3D structures, it was also used to study the thermal conductivity of 2D  $\text{MAPbI}_3$  thin films.<sup>26</sup> However, the resulted volume as a function of temperature curve from the MYP has discrepancies when compared to the experimental results because of the fact that the model ignored the charge redistribution and the covalent nature of lead iodide interactions.<sup>16</sup>

Hata *et al.*<sup>6</sup> studied  $\text{MAPbBr}_3$  using the same MYP potential developed by Mattoni *et al.*<sup>16</sup> They used the same Pb–Pb, Pb–MA, and MA internal interactions as in  $\text{MAPbI}_3$ . They calibrated the newly introduced parameters based on five scaling factors for developing a force-field for  $\text{MAPbBr}_3$ . Three of which were for scaling; namely:  $\alpha$  for coulomb–Buckingham parameters,  $\beta$  for the charges and  $\gamma$  for organic–inorganic interactions. Two additional factors resulted from the dynamics of phase transition which are  $A_{\text{OI}}$  and  $\rho_{\text{OI}}$  of  $\text{Br}^-$  (C, N). Although the developed model is simple, it reproduces, to a certain extent, the main static, and thermodynamic properties of  $\text{MAPbBr}_3$ .<sup>6,16</sup>  $\text{MAPbBr}_3$  has almost the same molecular dynamic behavior as  $\text{MAPbI}_3$ . However, the volume of  $\text{MAPbBr}_3$  is consistently smaller than that of  $\text{MAPbI}_3$ . The change of volume–temperature curve slope for  $\text{MAPbBr}_3$  is at 140–170 K compared to 150–200 K for  $\text{MAPbI}_3$ . This is attributed to the orthorhombic-to-tetragonal phase transition as mentioned by Mattoni *et al.*<sup>16</sup> Moreover, the anisotropy in the orthorhombic phase, longest to shortest lattice parameter ratio, of  $\text{MAPbBr}_3$  is slightly higher than that of  $\text{MAPbI}_3$  but still is underestimated relative to the experimental value. However, it is overestimated for  $\text{MAPbI}_3$ . In fact, for both  $\text{MAPbBr}_3$  and  $\text{MAPbI}_3$ , the calculated anisotropy does not change upon the phase transition from tetragonal to cubic which can be understood from the limitations of the two-body potentials for inorganic lattices. Still, by calibrating mixed I–Br interactions, it would be possible to model the large class of mixed systems  $\text{MAPb}(\text{I}_{1-x}\text{Br}_x)_3$ .<sup>6</sup>

Molecular dynamics simulations were used to study the effect of moisture on  $\text{MAPI}_3$  which is highly hydrophilic. A MYP-based force field (MYP1) for water–MAPI systems was developed to study the dissolution of  $\text{MAPbI}_3$  crystals in water.<sup>27</sup> It was further used to clarify that the apparent hydrophobic experimental contact angle resulted from the surface degradation during measurement.<sup>28</sup> Despite the accuracy of the models developed by Mattoni *et al.*<sup>16</sup> and Hata *et al.*,<sup>6</sup> these models cannot predict the complex crystal structure transitions and they are not transferrable to mixed halides perovskites  $\text{MAPb}(\text{I}_{1-x}\text{Br}_x)_3$ .

Handley and Freeman<sup>29</sup> also presented a set of interatomic potentials for modelling  $\text{MAPbI}_3$  that included short-range



interactions for the lead and iodide interactions to improve the degree of transferability. Artificial intelligence algorithms, such as artificial neural networks (ANNs) and genetic algorithms (GAs) were employed to develop force fields that represented the mixed halide perovskites. Chen and Pao<sup>30</sup> used artificial neural networks (ANN) to model complex structures and transitions. They demonstrated that by developing an ANN potential for MAPbI<sub>3</sub> as an example. Marchenko *et al.*<sup>31</sup> developed a semi-empirical model that represents the mixed halides hybrid perovskites and they used it to calculate Gibbs free energy and thermodynamic properties. Balestra *et al.*<sup>32</sup> used genetic algorithms to adjust the Coulomb–Buckingham pair atomic potentials to model the mixed halide systems of CsPb(I<sub>x</sub>Br<sub>1−x</sub>)<sub>3</sub>. They used their modified potential values to reproduce the DFT calculations of the lattice geometric distortions energies. However, their modified force field was fitted only to cubic structures of CsPbI<sub>3</sub>, CsPbBr<sub>3</sub>, and mixed CsPbI<sub>3</sub>Br with the aim to be transferable between them. The radial distribution function of the cubic CsPbI<sub>3</sub> was successfully obtained and matched the experimental results.<sup>32</sup> However, the new derived force field acceptably agreed with experiments and previous theoretical studies of structural and dynamic properties, particularly, for the pure structures, *i.e.*, the non-mixed, in their cubic crystalline structure form.

Although, the inorganic metal halide perovskites, particularly CsPbI<sub>3</sub>, have unique properties and better stability than MAPbI<sub>3</sub>, their structural properties, and phase transitions are not well-characterized and further investigation is needed. Therefore, the objective of this work is to apply molecular dynamics to investigate the structural properties and phase transformation of CsPbI<sub>3</sub> by applying the proper force field. We achieved this by introducing a novel hybrid force field which is referred to as “Hybrid EABC”, where EABC stands for Embedded-Atomic-Method and Buckingham–Coulomb potential. We compared the outcomes of using both Coulomb–Buckingham potential and Hybrid EABC in reproducing the experimentally reported and the *ab initio* structure's radial distribution functions and phase transitions of CsPbI<sub>3</sub> with an ultimate aim to gain in-depth understanding of the CsPbI<sub>3</sub> to further enhance its properties.

## Methodology

Molecular dynamics simulations require the initial positions of atoms, which we obtained from our DFT calculations and the force field as inputs. We discuss the application of two force fields. The first force field follows the Buckingham–Coulomb representation which is an interatomic pair potential. The second force field is Hybrid EABC, which is based on the application of interatomic pair potentials combined with the Embedded Atomic Method (EAM). We also present the simulation details and discuss the outputs.

### The orthorhombic structure from DFT simulation

The input structures for the classical MD were obtained from the DFT electronic and ionic energy minimization using PAW-

GGA with a cutoff energy of 520 eV using Vienna *Ab initio* Simulation Package VASP.<sup>33,34</sup> The FAST algorithm was employed for the electronic minimization with a stopping criterion of  $1 \times 10^{-4}$  eV. The ionic relaxation was set to stop if all forces are smaller than  $0.02 \text{ eV } \text{\AA}^{-1}$ . The resulting orthorhombic structure of CsPbI<sub>3</sub> is composed of 20 atoms and has lattice parameters of 4.902, 10.771, and 18.211 Å as illustrated using VESTA<sup>35</sup> in Fig. 1.

### Buckingham–Coulomb pair potential

We used Buckingham–Coulomb potential ( $U_{\text{BC}}$ ) to model the pair atomic interactions due to the inorganic nature of CsPbI<sub>3</sub> bonds. This potential is used effectively in studying inorganic and ionic crystals.<sup>17</sup> The general schematic of Buckingham–Coulomb interactions is shown in Fig. 2.

Buckingham–Coulomb potential ( $U_{\text{BC}}$ ) is numerically more stable than the Lennard-Jones potential.<sup>36</sup> In Buckingham–Coulomb potential ( $U_{\text{BC}}$ ), the long-term coulomb interaction is added to Buckingham potential as shown in eqn (3).

$$U_{\text{BC}}(r_{ij}) = A_{ij}e^{-\frac{r_{ij}}{\rho_{ij}}} - \frac{C_{ij}}{r_{ij}^6} + \frac{q_i q_j}{4\pi\epsilon_0 r_{ij}} \quad (3)$$

where,  $r_{ij}$  is the distance between atoms  $i$  and  $j$ ,  $q_i$  and  $q_j$  are their respective effective charges, and  $A_{ij}$ ,  $\rho_{ij}$  and  $C_{ij}$  are the Buckingham potential parameters of the pair atoms  $i$  and  $j$ .<sup>37</sup>

The potential parameters for the six interactions are required to completely define the force field between the constituent ions of CsPbI<sub>3</sub> perovskite. For the parameters of Cs–Cs and Cs–I Interactions, the Buckingham parameters were obtained from Sangster and Atwood.<sup>38</sup> For Cs–Pb, interaction, we used Mirskaya technique which is based on the geometric mean combining rule for the total interaction energy of two non-bonded atoms for the Buckingham potential and shown in eqn (4) and (5).<sup>39</sup>

$$A_{\text{Cs–Pb}} = \sqrt{A_{\text{Cs–Cs}} \times A_{\text{Pb–Pb}}} \quad (4)$$

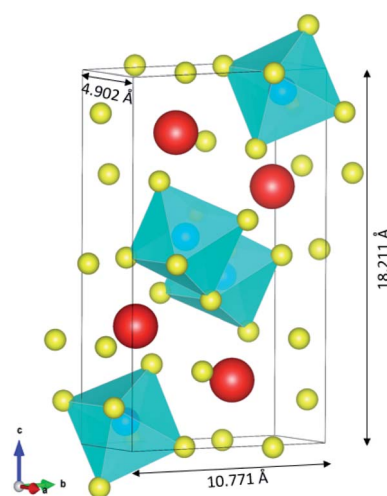


Fig. 1 The resulting orthorhombic structure of CsPbI<sub>3</sub> from DFT. The structure is composed of 4 Cs atoms (in red color), 4 Pb atoms (in blue color) and 12 I atoms (in yellow color).



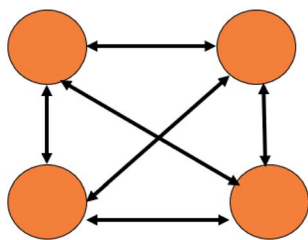


Fig. 2 Schematic representation of pair potential interactions.

$$\rho_{\text{Cs-Pb}} = \frac{2\rho_{\text{Cs-Cs}} \times \rho_{\text{Pb-Pb}}}{\rho_{\text{Cs-Cs}} + \rho_{\text{Pb-Pb}}} \quad (5)$$

For  $C_{\text{Cs-Pb}}$ , an iterative algorithm was developed to find the ideal value. This value was approximately the same value for  $C_{\text{Cs-Pb}}$  that was obtained by Mirskaya<sup>39</sup> method from  $C_{\text{Cs-Cs}}$  and  $C_{\text{Pb-Pb}}$  by Balestra *et al.*<sup>32</sup> For the parameters of Pb-Pb, Pb-I, and I-I interactions, they were set to be equal to the ones in MYP.<sup>16,18</sup> The effective charge of  $\text{Cs}^+$  was assumed to be the same charge of  $\text{MA}^+$  as in  $\text{MAPbI}_3$ .<sup>18</sup> These interactions along with the effective charges are summarized in Table 1.

### Hybrid EABC potential

Although pair interatomic potentials are simple and adequately model the material behavior, they do not reflect the true nature of bonds. They overestimate the vacancy formation and fail in predicting the crystal structure of metals and modelling surface relaxation behavior.<sup>40</sup> This is expected as all the higher terms of atomic interactions are neglected.<sup>13,40</sup>

Therefore, in this work, we developed a new potential of  $\text{CsPbI}_3$  by superimposing the Embedded Atomic Method (EAM) to BC pair potential to model both Cs-Cs and Pb-Pb interactions to reflect the metallic nature of these bonds. The EAM potential was first developed in 1984 by Daw and Baskes to study the hydrogen embrittlement in metals.<sup>41</sup> EAM potential ( $U_{\text{EAM}}$ ) adds the embedding energy, which simply represents the energy required to embed positively charged atomic cores into the electron density, to the pair atomic potential. The EAM is presented schematically in Fig. 3.

The EAM potential can successfully model the cohesion, defects, surface relaxation, and ground-state impurity energies

Table 1 Coulomb–Buckingham potential model parameters of  $\text{CsPbI}_3$

Interaction	A (eV)	$\rho$ (Å)	C (eV Å <sup>6</sup> )	Ion	Effective charge
Cs–Cs	$3.584 \times 10^{16}$	0.0843	240.34	Cs	1.36
Cs–Pb	$3.3068 \times 10^{11}$	0.10519	480.0		
Cs–I	4913.000	0.3814	480.06	Pb	2.03
Pb–Pb	3 051 120.5	0.131258	0.0		
Pb–I	4488.05	0.321737	0.0	I	−1.13
I–I	988.42	0.482217	30.22285		

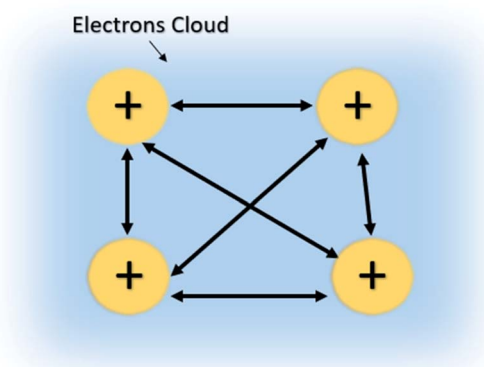


Fig. 3 Schematic representation of embedded atomic method force field.

resulting in overcoming the limitations of pair potentials.<sup>13,40,42</sup> In general, it improves the potential performance dramatically and still could be applied to large systems. The EAM potential ( $U_{\text{EAM}}$ ) is estimated using eqn (6) and (7) in terms of the pair potential and embedding energy as a function of electron density.

$$U_{\text{EAM}} = \frac{1}{2} \sum_{i \neq j} U_{ij}(r_{ij}) + \sum_i F_i(\bar{\rho}_i) \quad (6)$$

$$\bar{\rho}_i = \sum_{j \neq i} \rho_j(r_{ij}) \quad (7)$$

where,  $U_{ij}(r_{ij})$  is the pair atomic interactions,  $F(\bar{\rho}_i)$  is the energy required to insert the ionic cores into the electron density and represents the many-body behavior. The  $\bar{\rho}_i$  is the average total contribution from all atoms to the electron density at the position of atom  $i$ , and the  $\rho_j$  is the electron density contribution of atom  $j$ .<sup>13,40,42</sup>

In our new proposed Hybrid EABC potential, for the interactions between Cs–Cs and Pb–Pb, the Buckingham part of the potential shown in eqn (3) is replaced by the EAM potential shown in eqn (6)<sup>43,44</sup> while the Coulomb potential is still imposed. The new Hybrid EABC potential parameters are summarized in Table 2.

### Molecular dynamics simulations

All classical molecular dynamics calculations were carried by Linear Atomic/Molecular Massive Parallel Simulator (LAMMPS).<sup>45</sup> The bulk elements of 1920 atoms were generated by duplicating the unit cell  $6 \times 4 \times 4$  by ATOMSK code<sup>46</sup> and periodic boundary conditions were applied. The supercell visualization was carried out by OVITO.<sup>47</sup> For both force fields (BC and Hybrid EABC), the cutoff radii were set to be 12 Å based on iterations to produce the most stable structure at room temperature. First, the system was equilibrated at ambient conditions (300 K and 1 atm), with a time step of 0.5 femto-seconds (fs) for 30 picoseconds (ps) to study the density and structural properties at ambient conditions. Then, temperature was increased to study the phase transition. This was achieved





Table 2 Hybrid-EABC potential model parameters of CsPbI<sub>3</sub>

Hybrid EABC interactions	A (eV)	$\rho$ (Å)	C (eV Å <sup>6</sup> )	Ion	Effective charge
Cs–Pb	$3.3068 \times 10^{11}$	0.10519	0.0	Cs, Pb, I	1.36, 2.03, –1.13
Cs–I	4913.000	0.3814	480.06		
Pb–I	4488.05	0.321737	0.0		
I–I	988.42	0.482217	30.22285		
<b>Coul–EAM</b>	<b>Buck</b>	<b>EAM</b>	<b>Coul</b>		
Cs–Cs	0	Ref. 43	Cs <sup>1.36+</sup>		
Pb–Pb	0	Ref. 44	Pb <sup>2.03+</sup>		

by the isobaric–isothermal NPT ensemble which applied Nose–Hoover thermostat and barostat.<sup>48</sup> In the case of the Buckingham–Coulomb potential, the temperature was raised at a rate of 100 K every 16 ps. However, in the case of the new proposed Hybrid EABC, the temperature was increased at a rate of 100 K every 48 ps to ensure proper equilibration and temperature control. For every 100 timesteps, the temperature, density, and simulation box edges were reported.

The CMD simulations outputs were the radial pair distribution function,  $g_{\alpha\beta}(r)$ , and the change of density with the temperature. The  $g_{\alpha\beta}(r)$  was calculated after the relaxation at room temperature conditions using eqn (8).

$$g_{\alpha\beta}(r) = \frac{\langle n_{\alpha\beta}(r) \rangle \Delta r}{4\pi r^2 \rho c_{\beta}} \quad (8)$$

where,  $n_{\alpha\beta}$  is the number of  $\beta$  atoms surrounding  $\alpha$  atoms,  $c_{\beta}$  is the fraction of the atoms  $\beta$  in the system,  $\rho$  is the number of atoms per unit volume,  $r$  is the distance from  $\alpha$  particle, and  $\Delta r$  is the shell thickness.<sup>49</sup>

The radial distribution function is a structural descriptor that represents the probability distribution of  $\beta$  particles surrounding another specific  $\alpha$  particle. The radial distribution function exhibits a series of discrete peaks in the case of a single crystal. In general, the magnitude and the location of the peaks depend on the exact crystal structure.<sup>49</sup>

## Results and discussion

The orthorhombic structure of a supercell that includes 1920 atoms of CsPbI<sub>3</sub>, was modeled and analyzed using the classical molecular dynamic LAMMPS software. Two force fields, Buckingham–Coulomb and the new proposed Hybrid EABC force were employed and their outputs are analyzed in this section. Among the outputs of the CMD simulations were the structure descriptors, such as the radial distribution functions, the interatomic distances, and the density. But, most importantly is the accurate description of the phase transformation and the melting of CsPbI<sub>3</sub>.

### Structure descriptors of CsPbI<sub>3</sub> at ambient conditions

The supercells of CsPbI<sub>3</sub> at the ambient condition from the CMD simulations using the Buckingham–Coulomb and the new proposed Hybrid EABC forces fields are illustrated in Fig. 4. It can be observed that the structure resulting from the Hybrid

EABC potential (Fig. 4b) is more ordered than the outcome of the Buckingham–Coulomb potential (Fig. 4a).

The radial distribution functions of bulk CsPbI<sub>3</sub> at 300 K using the Buckingham–Coulomb potential and Hybrid EABC potential were obtained using 100 bins and illustrated in Fig. 5 and 6 respectively. One significant difference between the outcomes of using the two potentials occurs in the Pb–I interaction, where the Buckingham–Coulomb peak is shifted to the right with  $\sim 0.15$  Å compared to the Hybrid EABC peak. Moreover, both peaks of Cs–Pb and Pb–I from the Hybrid EABC potential agree with the radial distribution functions resulted from the DFT calculations shown in Fig. 7, which implies that the inclusion of EAM potential in the Hybrid EABC helps to maintain the integrity of the initial orthorhombic structure. Moreover, the peaks resulting from using the hybrid potential are closer to the peaks of the radial distributions functions which were obtained experimentally<sup>50</sup> and are shown by the dotted red lines in Fig. 5 and 6.

The interatomic separation distances between the different ions using the Buckingham–Coulomb and Hybrid EABC potential functions were obtained from RDF with 1000 bins for higher accuracy and are reported in Table 3. When comparing the outcomes of the two force fields, the largest deviation occurs

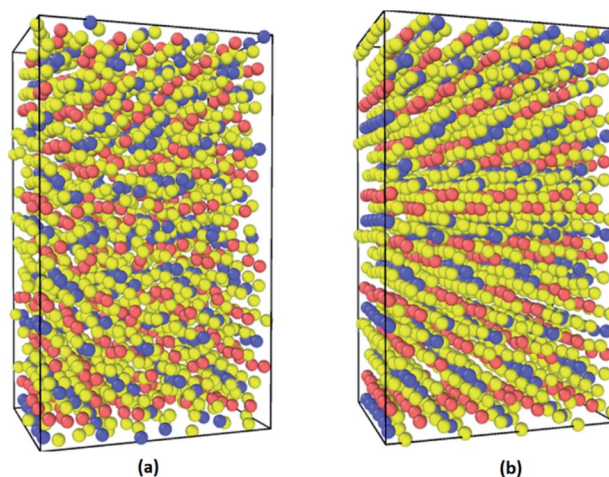


Fig. 4 The orthorhombic structures from CMD calculations at ambient conditions (yellow: I, red: Cs and blue: Pb) (a) orthorhombic structure after equilibration using Buckingham–Coulomb potential (b) orthorhombic structure after equilibration using Hybrid EABC potential.



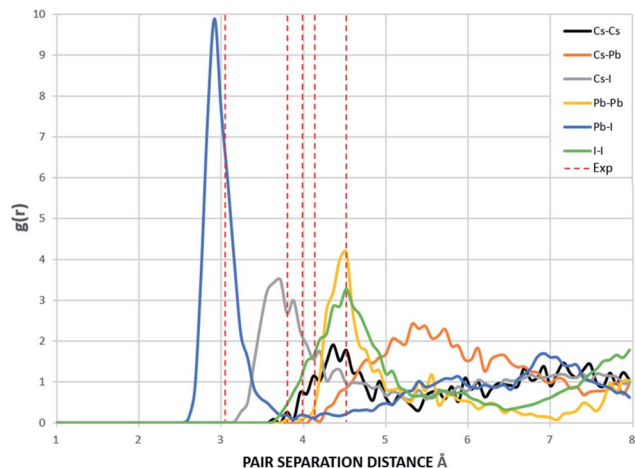


Fig. 5 The radial distribution function of the equilibrated structure with Buckingham–Coulomb at 300 K and  $g(r)$  with 100 bins (yellow: I, red: Cs and blue: Pb). The experimental values are obtained from ref. 50.

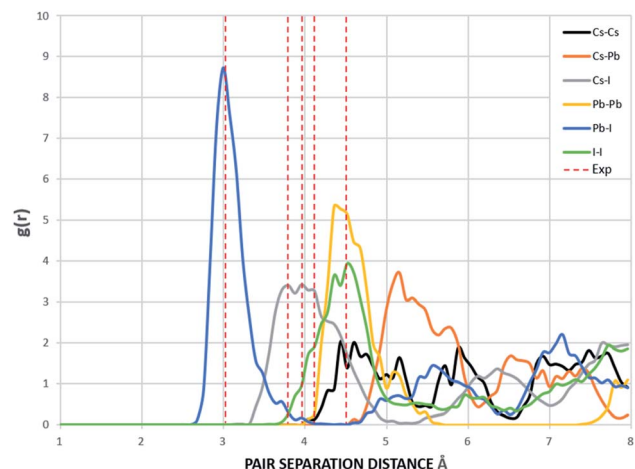


Fig. 6 The Radial distribution function of the equilibrated structure with Hybrid EABC at 300 K and  $g(r)$  with 100 bins (yellow: I, red: Cs and blue: Pb). The experimental values are obtained from ref. 50.

at the Cs–Pb interaction, where the Buckingham–Coulomb Cs–Pb peak is shifted  $\sim 0.4$  Å to the left of the Hybrid EABC peak. Whereas the least deviations occur at Cs–Cs and I–I peaks with a deviation of  $\sim 0.01$  Å.

In fact, the new proposed Hybrid EABC results in Pb–I bond lengths of  $\sim 3.05$  Å which agrees with experimental findings reported by Straus *et al.*<sup>50</sup> with an error of less than 1%. Also, it proves that the change in lattice parameters with temperature must originate from tilting in the octahedra of Pb–I. The accuracy of modelling Pb–I interaction is crucial in modelling lead iodide perovskites as the electronic and optical properties are greatly dependent on this interaction.<sup>7</sup>

It is worth noting that when the structure was equilibrated with the Hybrid-EABC force field but with omitting the Cs–Cs and Pb–Pb coulomb interactions, the orthorhombic structure clustered into CsI and PbI<sub>2</sub> as shown in Fig. 8. This

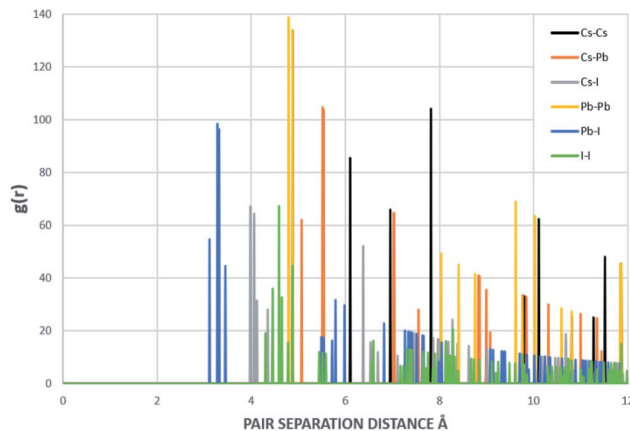


Fig. 7 Radial distribution function of the structure that resulted from DFT and input to MD. This RDF was generated with 1000 bins.

Table 3 Atomic separation distance between the ions with 1000 bins

Interaction	Interatomic distance (Å)	
	Coul–Buck	Hybrid EABC
Cs–Cs	4.4820	4.4700
Cs–Pb	5.3820	4.9860
Cs–I	3.6900	3.7500
Pb–Pb	4.4820	4.5180
Pb–I	2.9100	3.0540
I–I	4.5180	4.5060

demonstrates the experimental method of mixing CsI and PbI<sub>2</sub> (ref. 9) to produce CsPbI<sub>3</sub> but in reverse. Also, this implies the significance of coulombic interactions between Cs–Cs and Pb–Pb in stabilizing the structure.

The scatter plots of the X-positions vs. Z-positions of CsPbI<sub>3</sub> ions within the supercell at 0 K, 300 K and 600 K are shown in Fig. 9. A clear rattling behavior appeared in the scatter plot of the X-positions vs. Z-positions of at 300 K when compared to 0 K. This behavior can be attributed to the distortion of Cs

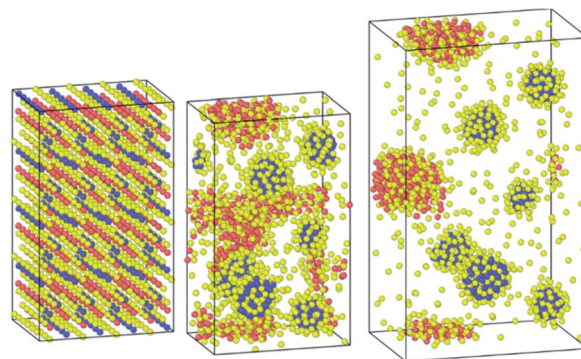


Fig. 8 Clustering of CsPbI<sub>3</sub> as CsI and PbI<sub>2</sub> when the coulombic interactions are neglected between cesium ions and between lead atoms.



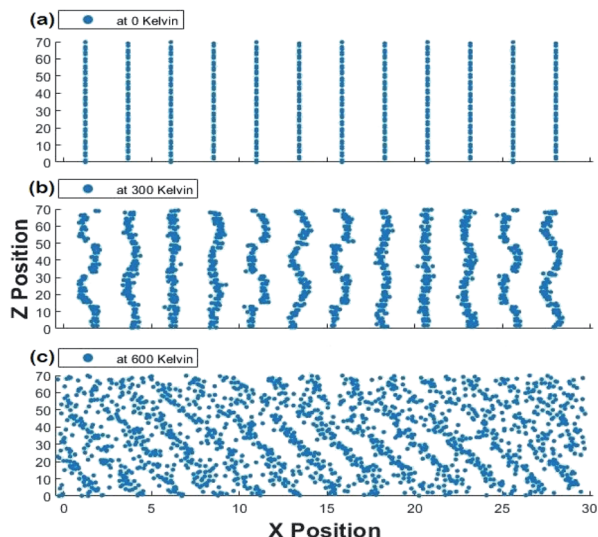


Fig. 9 Scatter plot of X positions vs. Z positions for the 1920 atoms at (a) 0 K, (b) 300 K and (c) 600 K at one time for the Hybrid EABC model.

atoms and Pb–I octahedra. The highly distorted and irregular behavior of Cs ions can also be observed in our Cs–Cs interaction in the RDF results shown in Fig. 5 and 6. This agrees with the findings in ref. 50 that Cs cations become distorted, occupy two positions and rattle within the structure causing the instability of CsPbI<sub>3</sub> at ambient conditions. At 600 K, the increase in volume which is observed from the increase in the scattered positions along the X-axis indicates the transition into a cubic crystal structure and it would be discussed in more detail in the phase transformation section.

### The density of CsPbI<sub>3</sub> orthorhombic crystal structure

The density of the orthorhombic structure, resulting from our DFT calculations was 4.983 g cm<sup>−3</sup>. After the equilibration using the Buckingham–Coulomb force field at 300 K, the structure density decreased to approximately 4.8 g cm<sup>−3</sup>. On the other hand, when the full Hybrid EABC potential was used with 0.5 fs timestep, the density was 5.2558 g cm<sup>−3</sup>, which only 2.5% lower than the experimental value of orthorhombic  $\delta$ -CsPbI<sub>3</sub> in ref. 9 and 1.9% lower than the experimental value of orthorhombic  $\delta$ -CsPbI<sub>3</sub> in ref. 51.

### Phase transformation of CsPbI<sub>3</sub>

The change of density with temperature resulting from using the Buckingham–Coulomb (BC) potential is illustrated in Fig. 10. The density slowly decreases with temperature until a significant change in slope occurs at the vicinity of 800 K. This change in the slope could be attributed to the melting of CsPbI<sub>3</sub> indicated by Sharma *et al.*<sup>52</sup> However, this potential was not able to detect the transition from orthorhombic to cubic crystal structures obtained by Wang *et al.*<sup>9</sup>

When the new hybrid EABC was employed, the density vs. temperature curve exhibits an abrupt change of density at different temperatures indicating phase transformation as shown in Fig. 11. At 300 K, CsPbI<sub>3</sub> is stable as an orthorhombic

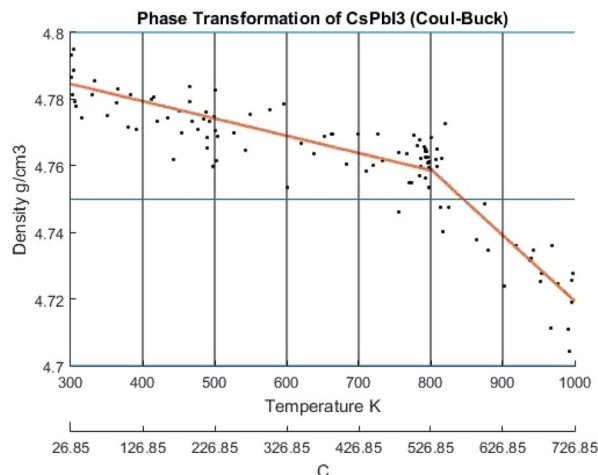


Fig. 10 The density of CsPbI<sub>3</sub> as a function of temperature calculated by Buckingham–Coulombs. The scatter points represent measured points from the CMD model and the orange curve is obtained by regression fitting.

structure with a density equal to 5.2558 g cm<sup>−3</sup>. Then, the density decreases gradually as the temperature increases to ~560 K and an abrupt decrease in density starts at ~610 K and it continues to decrease till it reaches 4.81 g cm<sup>−3</sup> at 630 K. This could be attributed to the phase transformation from the orthorhombic to cubic structure, *i.e.*  $\alpha$ -CsPbI<sub>3</sub>. This agrees within 1.5% with the experimental result by Trots *et al.*<sup>51</sup> which stated that CsPbI<sub>3</sub> undergoes orthorhombic-to-cubic phase transition through two stages. The first starts at 563 K where orthorhombic and cubic structures coexist and the other is at 602 K where only cubic structure is present. During this phase transition, an increase in volume by 7.5% occurs which is very comparable to the experimental value of 6.9% reported in ref. 51.

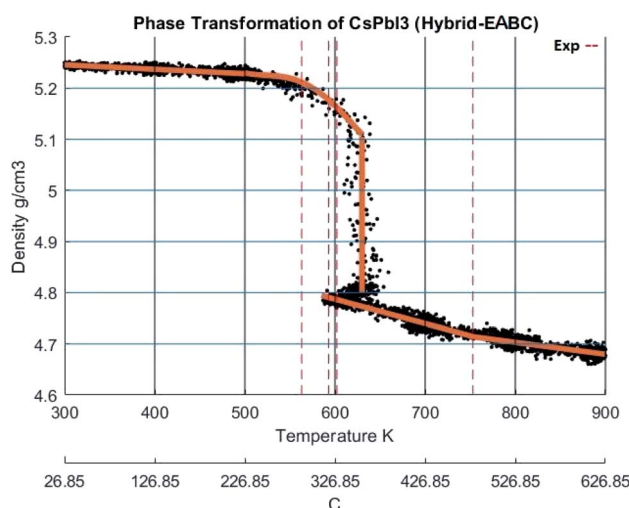


Fig. 11 The density of CsPbI<sub>3</sub> as a function of temperature calculated by Hybrid EABC. The scatter points represent measured points from the CMD model and the orange curve is obtained by regression fitting. The red dashed lines represent iso-temperature lines obtained from experimental values in ref. 9,51,52.





At 630 K, the density drops from 5.1 to 4.81 g cm<sup>-3</sup> while the system's Nose-Hoover thermostat was trying to maintain the system temperature at 600 K. This decrease in density along with the increase in volume was also observed in the scatter plot of the X-positions vs. Z-positions at 600 K shown previously in Fig. 9. Therefore, the system would eventually equilibrate at a density of 4.81 g cm<sup>-3</sup> at 600 K. The resulting structure is stable from ~593 K. The average temperature of the system from the beginning of the transformation till the end of the equilibration at the new phase is 594.6 K. These findings also perfectly match the experimental densities and the temperature reported by Wang *et al.*<sup>9</sup> and Trots *et al.*<sup>51</sup> and indicated by the dashed lines in Fig. 11. Further heating of the system results in a second change of slope at ~750 K which might be attributed to melting as reported by Sharma *et al.*<sup>52</sup>

## Conclusions

The inorganic halide perovskite cesium lead triiodide (CsPbI<sub>3</sub>) has been extensively researched for exceptional optoelectronic properties. However, an in-depth understating of its thermodynamic and structural stability was needed especially at higher temperatures when phase transformation occurs. In this paper, the molecular dynamics method was utilized to investigate the structural stability and the phase transformation of CsPbI<sub>3</sub>. The choice of the proper force fields significantly affects the accuracy of the model outputs. In this study, two force fields were tested: Buckingham-Coulomb and a newly developed force field called Hybrid EABC. Buckingham-Coulomb potential fails to reproduce the structure descriptors of CsPbI<sub>3</sub> or to predict its phase transition. This might happen because it considers only the pair interactions. On the other hand, the new Hybrid EABC potential which combined the embedded atomic method potential with the Buckingham-Coulomb potential reproduces the main structural and thermodynamics features of CsPbI<sub>3</sub>. The phase transformation from the orthorhombic to the cubic structure occurred at an average temperature of ~594 K with a density change from ~5.26 to 4.81 g cm<sup>-3</sup>. Therefore, the Hybrid EABC potential could be used to predict the dynamic interactions among the CsPbI<sub>3</sub> constituents and other properties including thermal conductivity, specific heat, and bulk modulus. This potential could also be utilized to investigate the structural stability and moisture sensitivity. Finally, the proposed Hybrid EABC potential can be extended to analyze other structures including the mixed-halides systems of CsPb(I<sub>x</sub>Br<sub>1-x</sub>)<sub>3</sub>.

## Conflicts of interest

There are no conflicts to declare.

## Acknowledgements

This work was supported by Penn State Materials Research Institute (MRI) and Penn State Institutes of Energy and Environment (IEE) seed grant. Computations for this research were

performed on the Pennsylvania State University's Institute for Computational and Data Sciences' Roar supercomputer.

## References

- 1 A. Smets, K. Jäger, O. Isabella, R. Van Swaaij and M. Zeman, *Solar Energy: the physics and engineering of photovoltaic conversion, technologies and systems*, Cambridge: UIT, 2015.
- 2 Q. Li, L. Zhang, Z. Chen and Z. Quan, Metal halide perovskites under compression, *J. Mater. Chem. A*, 2019, 7(27), 16089–16108.
- 3 B. Li, W. Hui, X. Ran, Y. Xia, F. Xia, L. Chao, Y. Chen and W. Huang, Metal halide perovskites for resistive switching memory devices and artificial synapses, *J. Mater. Chem. C*, 2019, 7(25), 7476–7493.
- 4 *Best Research-Cell Efficiency Chart*, available, <https://www.nrel.gov/pv/cell-efficiency.html>.
- 5 S. Patwardhan, D. H. Cao, S. Hatch, O. K. Farha, J. T. Hupp, M. G. Kanatzidis and G. C. Schatz, Introducing perovskite solar cells to undergraduates, *J. Phys. Chem. Lett.*, 2015, 6(2), 251–255.
- 6 T. Hata, G. Giorgi, K. Yamashita, C. Caddeo and A. Mattoni, *Development of a classical interatomic potential for MAPbBr<sub>3</sub>*, 2017.
- 7 H. Fujiwara and R. W. Collins, *Spectroscopic Ellipsometry for Photovoltaics*, Springer, Switzerland, 2018.
- 8 J. Duan, H. Xu, W. E. I. Sha, Y. Zhao, Y. Wang, X. Yang and Q. Tang, Inorganic perovskite solar cells: an emerging member of the photovoltaic community, *J. Mater. Chem. A*, 2019, 7(37), 21036–21068.
- 9 B. Wang, N. Novendra and A. Navrotsky, Energetics, structures, and phase transitions of cubic and orthorhombic cesium lead iodide (CsPbI<sub>3</sub>) polymorphs, *J. Am. Chem. Soc.*, 2019, 141(37), 14501–14504.
- 10 D. L. Busipalli, K. Y. Lin, S. Nachimuthu and J. C. Jiang, *Enhanced moisture stability of cesium lead iodide perovskite solar cells—a first-principles molecular dynamics study*, 2020.
- 11 C. Paduani and A. M. Rappe, Tuning the gap of lead-based halide perovskites by introducing superalkali species at the cationic sites of ABX<sub>3</sub>-type structure, *Phys. Chem. Chem. Phys.*, 2017, 19(31), 20619–20626.
- 12 C. Motta, F. El-Mellouhi and S. Sanvito, Exploring the cation dynamics in lead-bromide hybrid perovskites, *Phys. Rev. B*, 2016, 93(23), 235412.
- 13 J. G. Lee, *Computational materials science: an introduction*, 2011.
- 14 F. Giustino, *Materials modelling using density functional theory: properties and predictions*, 2014.
- 15 D. C. Rapaport and D. C. R. Rapaport, *The art of molecular dynamics simulation*, Cambridge university press, 2004.
- 16 A. Mattoni, A. Filippetti, M. I. Saba and P. Delugas, *Methylammonium rotational dynamics in lead halide perovskite by classical molecular dynamics: the role of temperature*, 2015.
- 17 M. Matsui, *Molecular dynamics study of MgSiO<sub>3</sub> perovskite*, 1988.





- 18 A. Mattoni, A. Filippetti and C. Caddeo, *Modeling hybrid perovskites by molecular dynamics*, 2016.
- 19 S. Maheshwari, M. B. Fridriksson, S. Seal, J. Meyer and F. C. Grozema, The Relation between Rotational Dynamics of the Organic Cation and Phase Transitions in Hybrid Halide Perovskites, *J. Phys. Chem. C*, 2019, **123**(23), 14652–14661.
- 20 P. Delugas, C. Caddeo, A. Filippetti and A. Mattoni, Thermally activated point defect diffusion in methylammonium lead trihalide: anisotropic and ultrahigh mobility of iodine, *J. Phys. Chem. Lett.*, 2016, **7**(13), 2356–2361.
- 21 J. Wang, L. Zhao, M. Wang and S. Lin, Molecular Insights into Early Nuclei and Interfacial Mismatch during Vapor Deposition of Hybrid Perovskites on Titanium Dioxide Substrate, *Cryst. Growth Des.*, 2017, **17**(12), 6201–6211.
- 22 C. Wang, Y. Liu, S. F. Liu, B. Li and Y. Chen, Giant phonon tuning effect *via* pressure-manipulated polar rotation in perovskite MAPbI<sub>3</sub>, *J. Phys. Chem. Lett.*, 2018, **9**(11), 3029–3034.
- 23 J. Ma and L. W. Wang, The nature of electron mobility in hybrid perovskite CH<sub>3</sub>NH<sub>3</sub>PbI<sub>3</sub>, *Nano Lett.*, 2017, **17**(6), 3646–3654.
- 24 C. G. Bischak, A. B. Wong, E. Lin, D. T. Limmer, P. Yang and N. S. Ginsberg, Tunable polaron distortions control the extent of halide demixing in lead halide perovskites, *J. Phys. Chem. Lett.*, 2018, **9**(14), 3998–4005.
- 25 A. Mattoni and C. Caddeo, Dielectric function of hybrid perovskites at finite temperature investigated by classical molecular dynamics, *J. Chem. Phys.*, 2020, **152**(10), 104705.
- 26 A. Giri, A. Chen, A. Mattoni, K. Aryana, D. Zhang, X. Hu, S. Lee, J. Choi and P. Hopkins, Ultralow thermal conductivity of two-dimensional metal halide perovskites, *Nano Lett.*, 2020, **20**(5), 3331–3337.
- 27 C. Caddeo, M. I. Saba, S. Meloni, A. Filippetti and A. Mattoni, Collective molecular mechanisms in the CH<sub>3</sub>NH<sub>3</sub>PbI<sub>3</sub> dissolution by liquid water, *ACS Nano*, 2017, **11**(9), 9183–9190.
- 28 C. Caddeo, D. Marongiu, S. Meloni, A. Filippetti, F. Quochi, M. Saba and A. Mattoni, Hydrophilicity and Water Contact Angle on Methylammonium Lead Iodide, *Adv. Mater. Interfaces*, 2019, **6**(3), 1801173.
- 29 C. M. Handley and C. L. Freeman, A new potential for methylammonium lead iodide, *Phys. Chem. Chem. Phys.*, 2017, **19**(3), 2313–2321.
- 30 H. A. Chen and C. W. Pao, Fast and Accurate Artificial Neural Network Potential Model for MAPbI<sub>3</sub> Perovskite Materials, *ACS Omega*, 2019, **4**(6), 10950–10959.
- 31 E. I. Marchenko, S. A. Fateev, A. A. Petrov, E. A. Goodilin, N. N. Eremin and A. B. Tarasov, Transferable Approach of Semi-Empirical Modeling of Disordered Mixed-Halide Hybrid Perovskites CH<sub>3</sub>NH<sub>3</sub>Pb (1–x Br x)<sub>3</sub>: Prediction of Thermodynamic Properties, Phase Stability, and Deviations from Vegard's Law, *J. Phys. Chem. C*, 2019, **123**(42), 26036–26040.
- 32 S. R. G. Balestra, J. M. Vicent-Luna, S. Calero, S. Tao and J. A. Anta, *Efficient Modelling of Ion Structure and Dynamics in Inorganic Metal Halide Perovskites*, 2020.
- 33 G. Kresse and J. Furthmüller, Efficient iterative schemes for *ab initio* total-energy calculations using a plane-wave basis set, *Phys. Rev. B*, 1996, **54**, 11169.
- 34 G. Kresse and D. Joubert, From ultrasoft pseudopotentials to the projector augmented-wave method, *Phys. Rev. B*, 1999, **59**, 1758.
- 35 K. Mommda and F. Izumi, VESTA 3 for three-dimensional visualization of crystal, volumetric and morphology data, *J. Appl. Crystallogr.*, 2011, **44**, 1272–1276.
- 36 F. Jensen, *Introduction to computational chemistry*, John Wiley & sons, 2017.
- 37 R. A. Buckingham, *The classical equation of state of gaseous helium, neon and argon*, 1938.
- 38 M. J. L. Sangster and R. M. Atwood, Interionic potentials for alkali halides. II. Completely crystal independent specification of Born-Mayer potentials, *J. Phys. C: Solid State Phys.*, 1978, **11**(8), 1541.
- 39 K. Mirskaya, *Combining rules for interatomic potential functions of Buckingham form*, 1973.
- 40 M. S. Daw, S. M. Foiles and M. I. Baskes, *The embedded-atom method: a review of theory and applications*, 1993.
- 41 M. S. Daw and M. I. Baskes, Embedded-atom method: Derivation and application to impurities, surfaces, and other defects in metals, *Phys. Rev. B*, 1984, **29**(12), 6443.
- 42 R. LeSar, *Introduction to computational materials science: Fundamentals to applications*, 2013.
- 43 A. Nichol and G. Ackland, Property trends in simple metals: An empirical potential approach, *Phys. Rev. B*, 2016, **93**(18), 184101, DOI: 10.1103/physrevb.93.184101.
- 44 K. Wang, W. Zhu, M. Xiang, Y. Xu, G. Li and J. Chen, Improved embedded-atom model potentials of Pb at high pressure: application to investigations of plasticity and phase transition under extreme conditions, *Modell. Simul. Mater. Sci. Eng.*, 2018, **27**(1), 015001.
- 45 S. Plimpton, *Fast Parallel Algorithms for Short-Range Molecular Dynamics*, 1995.
- 46 P. Hirel, Atomsk: A tool for manipulating and converting atomic data files, *Comput. Phys. Commun.*, 2015, **197**, 212–219.
- 47 A. Stukowski, Visualization and analysis of atomistic simulation data with OVITO—the Open Visualization Tool, *Modell. Simul. Mater. Sci. Eng.*, 2009, **18**(1), 015012.
- 48 S. Nosé, A unified formulation of the constant temperature molecular dynamics methods, *J. Chem. Phys.*, 1984, **81**(1), 511–519.
- 49 J. G. Kirkwood and E. M. Boggs, The radial distribution function in liquids, *J. Chem. Phys.*, 1942, **10**(6), 394–402.
- 50 D. B. Straus, S. Guo, M. Abeykoon and R. J. Cava, Understanding the Instability of the Halide Perovskite CsPbI<sub>3</sub> through Temperature-Dependent Structural Analysis, *Adv. Mater.*, 2020, **32**, 2001069.
- 51 D. M. Trots and S. V. Myagkota, High-temperature structural evolution of caesium and rubidium triiodoplumbates, *J. Phys. Chem. Solid.*, 2008, **69**(10), 2520–2526.
- 52 S. Sharma, N. Weiden and A. Weiss, Phase diagrams of quasibinary systems of the type: ABX<sub>3</sub>—A' BX<sub>3</sub>; ABX<sub>3</sub>—AB' X<sub>3</sub>, and ABX<sub>3</sub>—ABX' <sub>3</sub>; X= halogen, *Z. Phys. Chem.*, 1992, **175**(1), 63–80.

